Coupled oscillations of the Wilberforce pendulum unveiled by smartphones

Thomas Gallot*
Instituto de Física, Facultad de Ciencias, UdelaR, Iguá 4225, 11200, Uruguay

Daniel Gau†
Instituto de Física, Facultad de Ingeniería, UdelaR, Av. Julio Herrera y Reissig 565, 11300, Uruguay

Rodrigo García-Tejera‡
Centre for Regenerative Medicine, University of Edinburgh, 5 Little France Dr, Edinburgh EH16 4UU, U.K. and Instituto de Física, Facultad de Ciencias, UdelaR, Iguá 4225, 11200, Uruguay

The Wilberforce pendulum illustrates important properties of coupled oscillators including normal modes and beat phenomena. When helical spring is attached to a mass to create the Wilberforce pendulum, the longitudinal and torsional oscillations are coupled. A Wilberforce and be constructed simply from a standard laboratory spring and a can, and a smartphone's accelerometer and gyroscope can be used to monitor the oscillations. We show that the resulting time-series data match theoretical predictions and we share procedures for observing both normal modes and beats.

I. INTRODUCTION

The oscillations of the Wilberforce pendulum have amazed people since they were first reported, at the end of the XIX century, by the British demonstrator in Physics L.R. Wilberforce[1]. In this simple device, consisting of a spiral spring attached to a mass, the linear and torsional modes of the system are coupled. When the frequencies of the two oscillation modes are closely spaced, they exchange energy producing a fascinating beat phenomenon.

The first reported analysis of the motion of the Wilberforce pendulum in real time was performed using an ultrasound distance sensor to detect the vertical motion of the mass[2]. There, the authors studied the beat phenomenon and analysed the motion of the system for each of the normal modes separately by applying different initial conditions to the system. This approach was then extended to include a digital video camera with the aim of detecting both the translational and rotational motion simultaneously[3]. Torzo et al. introduced a setup that was able to detect both motions simultaneously, using an ultrasonic distance sensor to detect the translational motion of the mass and a Non-Contact Rotation Sensor based on polarized light to measure the rotation angle[4]. More recently the detection of both movements using two cameras was also performed[5].

While the original purpose of the device was the measurement of spring constants, the Wilberforce pendulum is currently used in physics teaching at Universities to illustrate a wide variety of concepts regarding oscillatory phenomena as coupling, normal modes and[3,5–9]. In recent years the study of these fundamental concepts has been approached with the use of smartphones[10–15].

In this work, we present a new approach to study the Wilberforce pendulum using simultaneously the accelerometer and gyroscope of a smartphone, taking into account its significant contribution to the pendulum's mass and inertia. This device allows for the measurement of the accelerations and angular velocities. In section II we revisit the theory, discussing the mechanical basis of the coupling between the translational and torsional modes. We analyse the motion equations and derive analytically optimal initial conditions to observe the normal modes and beats. For the latter case, we prove that optimal beating in the accelerations is obtained through a zero-torque initial condition, rather than with the no-initial-rotation condition needed for beats in the position signals. In section III we describe our experimental setup, showing how to set the Wilberforce pendulum to optimal beating conditions. We outline our numerical experiments and present experimental results in agreement with simulations of the motion equations. The Python scripts for the experimental data analysis and numerical experiments are available on a GitHub repository[16].

II. MODELLING THE WILBERFORCE PENDULUM

We consider the setup depicted in Fig. 1, consisting of a Wilberforce pendulum with a smartphone attached at the bottom. To describe the motion of the system, we define the natural Cartesian coordinate system $(\hat{x}, \hat{y}, \hat{z})$ fixed to the smartphone, as shown in Fig. 1, and an angle θ representing the rotation from an initial resting point. Under this configuration, the traction-compression of the spring, (force F_z along the z-axis, see Fig. 2) generates a torque M_z inducing a shear stress in the

spring material. Reciprocally, the rotation of the spring (torque M_θ) generates a force F_θ inducing a traction-compression stress (bending) within the spring material. This observation is the core essence of the Wilberforce pendulum: the compression of the pendulum creates a rotational stress and, reciprocally, the rotation of the pendulum creates a compressional stress in the spring material, thus coupling the rotational and translational motions. A detailed analysis of the spring mechanics can be found in[17].

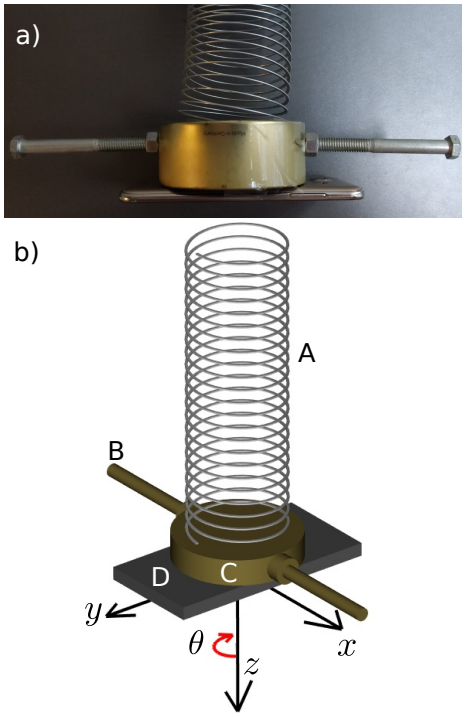

FIG. 1. Implementation of the Wilberforce pendulum. a) Profile picture of the pendulum's mass, spring and smartphone attached. b) Schematic of the Wilberforce pendulum consisting of **A.** the educational spring, **B.** bolts, **C.** cylindrical mass, and **D.** smartphone. The principal components of the motion are the translation z along the z-axis and rotation θ around the z-axis.

The elastic constant of a spring in traction/compression is given by $k = {}^{F_z}\!/_{z}$, being F_z the force after a displacement z along the z-axis.

Similarly, the rotational elastic constant is given by $\delta = {}^{M_\theta}\!/_{\theta}$, where M_θ is the torque associated with an angle variation θ around the z-axis. For a helical spring with N loops and diameter D, the spring constants can be calculated using strength mechanical theory[17,18], arriving at

$$\begin{aligned} k &= G\frac{I_z}{D^3}\frac{4}{N\pi} \\ \delta &= E\frac{I_\theta}{D}\frac{1}{N\pi}, \end{aligned} \tag{1}$$

where I_z and I_θ are the polar and axial moments of inertia, respectively[17]. Interestingly, the traction-compression elastic constant k depends on the shear modulus G of the spring material[18] that characterizes a rotational strain. Reciprocally, the torsional elastic constant δ is related to the Young's modulus E which characterizes a compressional strain. The elastic moduli, and thus the elastic constants, are connected by the Poisson's ratio ν: ${}^{E}\!/_{G} = 2(1+\nu)$. A traction-compression of the spring, (displacement along the z-axis) generates a torque within the spring material and, reciprocally, a rotation of the spring generates a traction-compression (bending), see Fig. 2. This observation is the core essence of the Wilberforce pendulum: the compression of the pendulum creates a rotational stress and, reciprocally, the rotation of the pendulum creates a compressional stress in the spring material, thus coupling the rotational and translational motions.

Considered independently, the translational and rotational motions have resonance frequencies, ω_z and ω_θ, that depend on the elastic constants and the mass m and moment of inertia I about the z-axis, namely

$$\begin{aligned} \omega_z &= \sqrt{{}^{k}\!/_{m}} \\ \omega_\theta &= \sqrt{{}^{\delta}\!/_{I}}. \end{aligned} \tag{2}$$

Such resonant frequencies cannot be measured directly due to the mechanical coupling between rotation and traction-compression; only the coupled system resonances can be measured. Moreover, even if m and I can be estimated independently, estimating the elastic constants k and δ can be challenging due to the coupling.

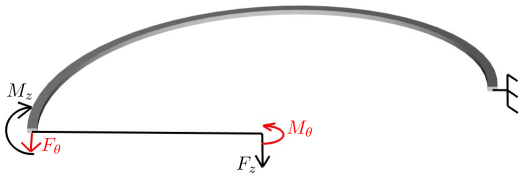

FIG. 2. Half-turn of a helical spring with rectangular cross-section. The force F_z along the z-axis associated with a translation z generates a torque $M_z = F_z D/2$ along the spring's cross-section. Reciprocally, the torque M_θ around the z-axis associated with a rotation θ generates a traction-compression force $F_\theta = 2M_\theta/D$ on the spring material.

A. Motion equations

Following Berg and Marshall[19], we consider a linear coupling between the resonators to describe the system dynamics in the absence of attenuation

$$\begin{cases} m\ddot{z} + kz + \frac{\epsilon}{2}\theta = 0 \\ I\ddot{\theta} + \delta\theta + \frac{\epsilon}{2}z = 0 \end{cases}, \tag{3}$$

where ϵ denotes the coupling strength, and z and θ the vertical and angular coordinate of the pendulum,

respectively, measured from their equilibrium points. Imposing the normal mode conditions $z(t) = A_z e^{i\omega t}$ and $\theta(t) = A_\theta e^{i\omega t}$, yields

$$\left(\omega_\theta^2 - \omega^2\right)\left(\omega_z^2 - \omega^2\right) = \frac{\epsilon^2}{4mI}. \tag{4}$$

The normal (eigen) frequencies of the coupled pendulum ω_1 and ω_2 are given by the two solutions of Eq. (4), yielding

$$\begin{aligned}\omega_1^2 =& \frac{\omega_\theta^2 + \omega_z^2}{2} + \frac{1}{2}\left[\left(\omega_\theta^2 - \omega_z^2\right)^2 + \frac{\epsilon^2}{mI}\right]^{1/2} \\ \omega_2^2 =& \frac{\omega_\theta^2 + \omega_z^2}{2} - \frac{1}{2}\left[\left(\omega_\theta^2 - \omega_z^2\right)^2 + \frac{\epsilon^2}{mI}\right]^{1/2}\end{aligned}. \tag{5}$$

Furthermore, introducing the perfect tuning hypothesis $\omega_\theta = \omega_z = \omega$, i.e., assuming that the fundamental frequencies for both oscillation types are equal, the normal frequencies read

$$\begin{aligned}\omega_1^2 =& \omega^2 + \omega\omega_B = \omega^2\left(1 + \frac{\omega_B}{\omega}\right) \\ \omega_2^2 =& \omega^2 - \omega\omega_B = \omega^2\left(1 - \frac{\omega_B}{\omega}\right),\end{aligned} \tag{6}$$

where we have introduced the beat frequency

$$\omega_B^2 = \frac{\epsilon^2}{4\omega^2 mI}. \tag{7}$$

Note that this equation allows for the calculation of ϵ from experimental measurements of ω, ω_B, m and I. Commonly, Eq. (6) is simplified by a binomial expansion for $\omega/\omega_B \ll 1$:

$$\begin{aligned}\omega_1 &= \omega + \omega_B/2 \\ \omega_2 &= \omega - \omega_B/2\end{aligned}. \tag{8}$$

Hence, ω represents the average normal frequency, and the beat frequency ω_B is the difference between the normal frequencies.

B. Optimum beating conditions

Following[19], we can condense the vertical $z(t)$ and angular $\theta(t)$ components of the movement in the vector $\hat{X}(t) = z(t)\,\hat{z} + \theta(t)\,\hat{\theta}$, where $\hat{z}$ and $\hat{\theta}$ are versors in the vertical and horizontal directions of motion, respectively. When the initial velocities are $\dot{z} = 0$ and $\dot{\theta} = 0$, the solution of the motion equations is given by the following superposition of normal modes $\hat{\eta}_1$ and $\hat{\eta}_2$

$$\hat{X}(t) = A_1\hat{\eta}_1 \cos\omega_1 t + A_2\hat{\eta}_2 \cos\omega_2 t. \tag{9}$$

The normal modes are given by

$$\begin{aligned}\hat{\eta}_1 =& \hat{\theta} + \hat{z}\sqrt{\frac{I}{m}} \\ \hat{\eta}_2 =& \hat{\theta} - \hat{z}\sqrt{\frac{I}{m}}.\end{aligned} \tag{10}$$

The amplitude of the normal modes are given by the initial conditions $z(0) = z_0$ and $\theta(0) = \theta_0$, yielding

$$\begin{aligned}A_1 =& \frac{1}{2}\left[\theta_0 + z_0\sqrt{\frac{m}{I}}\right] \\ A_2 =& \frac{1}{2}\left[\theta_0 - z_0\sqrt{\frac{m}{I}}\right]\end{aligned}. \tag{11}$$

A quick inspection of the amplitudes reveals that the first mode is symmetric, i.e., rotation and translation are in phase, while the second mode is anti-symmetric. Perfect beating takes place when both normal modes have the same amplitude, namely $A_1 = \pm A_2$. One of the initial conditions that generates beating motion is $\theta_0 = 0$, leading to the solutions

$$\begin{cases} z(t) = z_0 \cos\omega t \cos\frac{\omega_B}{2}t \\ \theta(t) = -z_0\sqrt{\frac{I}{m}} \sin\omega t \sin\frac{\omega_B}{2}t \end{cases}. \tag{12}$$

Under these conditions, the pendulum oscillates at the resonance frequency ω, and the oscillation is modulated by the beating frequency ω_B. Moreover, the rotational and translational oscillations have a $\pi/2$ phase difference, while the total energy remains constant. In order to compare the solutions to the motion equations to experimental data, it is worth noting that smartphones measure translational and rotational accelerations through their 3D accelerometers and gyroscopes, respectively[20]. For the motion described by Eq. (9), the corresponding accelerations are

$$\ddot{\hat{X}}(t) = -\omega_1^2 A_1\hat{\eta}_1 \cos\omega_1 t - \omega_2^2 A_2\hat{\eta}_2 \cos\omega_2 t. \tag{13}$$

Hence, the normal modes in acceleration conserve the same phase relationship than the displacements. However, it is important to note that the initial conditions for beating, $z_0 = 0$ or $\theta_0 = 0$ (with null initial velocities), do not yield accelerations with equal amplitudes for both frequencies, as it does with positions, but rather $A_1/A_2 = \omega_1^2/\omega_2^2$. In other words, the initial conditions that are necessary to observe beatings in the positional coordinates do not lead to beatings in the accelerations.

From Eq. (13), we observe that imposing a zero-initial-torque condition leads to beating in acceleration. Such condition be readily imposed experimentally by simply lifting the pendulum with one finger under its center of mass, up to the position in which the torque vanishes. The finger's position must enable free rotation. The initial angle for such condition can be found by imposing $\ddot{\theta} = 0$ in Eq. (3), leading to $\omega^2\theta_0 = -\frac{\epsilon}{2I}z_0$. Under these conditions, the observed accelerations are

$$\begin{cases} \ddot{z}(t) = -\omega^2\left(1 - \frac{\omega_B^2}{\omega^2}\right) z_0 \cos\omega t \cos\frac{\omega_B}{2}t \\ \ddot{\theta}(t) = \omega^2\left(1 - \frac{\omega_B^2}{\omega^2}\right) z_0\sqrt{\frac{m}{I}} \sin\omega t \sin\frac{\omega_B}{2}t \end{cases}, \tag{14}$$

thus showing perfect beating. On the other hand, the

observed positions for the same initial conditions are

$$\begin{cases} z(t) = z_0 \ \left(\cos\omega t \cos\frac{\omega_B}{2}t + \frac{\omega_B}{\omega}\sin\omega t \sin\frac{\omega_B}{2}t\right) \\ \theta(t) = -z_0\sqrt{\frac{m}{I}}\left(\sin\omega t \sin\frac{\omega_B}{2}t + \frac{\omega_B}{\omega}\cos\omega t \cos\frac{\omega_B}{2}t\right) \end{cases} . \tag{15}$$

We can see that, in addition to the main beating term, the positions have a term in anti-phase with respect to the main one, and proportional to $\frac{\omega_B}{\omega}$. As a consequence, the envelope of the positions has a minimum of $\frac{\omega_B}{\omega}$ instead of zero.

C. Modelling attenuation

The oscillations of a real Wilberforce pendulum are attenuated by friction. To model attenuation we can add damping terms as proposed in[5], to obtain the motion equations

$$\begin{cases} m\ddot{z} + \alpha_z\dot{z} + kz + \frac{\epsilon}{2}\theta = 0 \\ I\ddot{\theta} + \alpha_\theta\dot{\theta} + \delta\theta + \frac{\epsilon}{2}z = 0 \end{cases} . \tag{16}$$

Assuming a harmonic solution, the solutions of Eqs. (16) are the same than the solutions of Eqs. (3) for imaginary elastic constants $\tilde{k} = k + i\alpha_z$ and $\tilde{\delta} = \delta + i\alpha_\theta$. For the sake of simplicity, we assume that the intensity of the rotational and translational damping terms are equal, namely $\zeta = \frac{\alpha_z}{2m\omega} = \frac{\alpha_\theta}{2I\omega}$. Note that the natural frequency of both the translational and rotational oscillations are modified by a factor $\sqrt{1+i2\zeta}$, which can be approximated to $1+i\zeta$ when the attenuation is small enough, i.e., $\zeta << \omega$. We thus expect the analysis of the past section to remain valid even when attenuation is considered.

III. EXPERIMENT

The base of the pendulum depicted in Fig. 1 consists of a metallic hollow cylinder with an outer diameter of 9.5 cm. We added two 10.5 cm bolts and 4 nuts to increase the moment of inertia (2 nuts are inside the the cylinder). The cylinder was attached to a 7.0 cm-diameter spiral aluminium spring with a $2\times1\,\mathrm{mm}^2$ rectangular cross section, and 80 loops. We attached the spring to the ceiling and taped a $16\times8\,\mathrm{cm}^2$ smartphone to the box facing the ground, thus enabling access to the touch screen. The total moment of inertia of the system I was calculated by adding the moment of inertia of the components, and assuming that the density of each all elements was homogeneous. For the moment of inertia calculation, we considered the smartphone to be a rectangular prism, the bolts to be thin rods, and the cylinder as a thin shell. This way, the total moment of inertia is $I = (1925 \pm 6)\,10^{-6}\mathrm{kg\,m}^2$, and the mass of the pendulum is $m = (398.9 \pm 0.5)\,10^{-3}\mathrm{kg}$. For data acquisition, the smartphone recorded both accelerations and angular velocities in 3D. We used the application Phyphox® to read the smartphone accelerometer and gyroscope with a sampling frequency of $f_s = 10\,\mathrm{Hz}$[20]. Phyphox saves the the data in .csv format and e-mails it for further analysis on a PC, for which we built a very simple pipeline on Python.

A. Guidelines for experimental design

To securely fasten the pendulum's spring, smartphone, and an inertial element, a lightweight cylinder made of any suitable material can be used. Most smartphones have a convenient aspect ratio, with the screen length being twice the width, thereby contributing similarly to the moment of inertia. Additionally, the inertial component, which can be fashioned from a threaded rod or bolts, can be designed to fine-tune the pendulum, aiming for a close match between ω_θ and ω_z.

The mechanical parameters, namely mass (m), moment of inertia (I), and spring constant (k), can be estimated using a scale and a ruler. Estimating the parameter δ, however, would require a torque-measurement system. Moreover, the coupling between rotational and compressive forces render such measurement non-informative for tuning. Hence, to tune the pendulum, we recommend systematically adjusting the total length L of the inertial component until beatings are observed. As a starting point, we suggest setting the length of the pendulum to be four times the diameter of the spring: $L = 4D$. In our experimental setup, the mass of the smartphone is roughly twice the mass of the pair of rods and the length is set at $L = 28.5$ cm. The spring was suspended at a height of 2.3 m, and its stretched length measured 1.4 m, allowing for an observed oscillation with an amplitude of 0.82 m. This configuration leads to a relative difference between resonant frequencies of less than 3% (see Eq. (23)).

B. Estimating the position of the accelerometer

One of the advantages of our experimental setup over experiments based on video recordings is having easy access to a frame of reference attached to the pendulum. This allows for simultaneous measurements of the acceleration along the plane perpendicular to the spring's main axis by two different methods, which can be used to estimate the position of the accelerometer. The acceleration in the horizontal plane can be measured either by the accelerometer, which expresses it in the Cartesian coordinates x and y depicted in Fig. 1, or by the r, θ cylindrical coordinates, with $\dot{\theta}$ being the output of the gyroscope. The relationship between the accelerations lead to the estimation of the coordinates (r_a, θ_a) of the accelerometer.

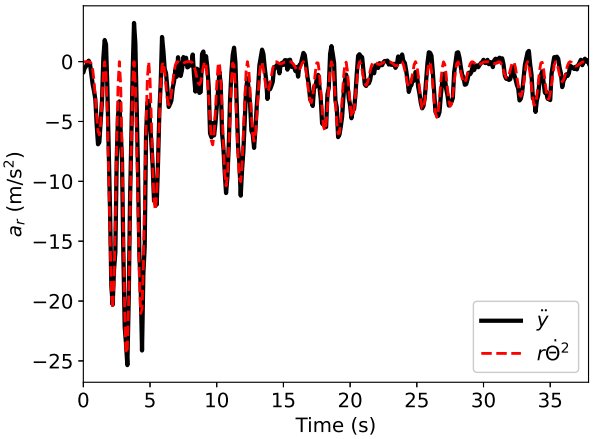

FIG. 3. Radial acceleration in the xy plane measured from the accelerometer and gyroscope outputs. Black line: acceleration along the $\vec{y}$ direction. This acceleration corresponds to the radial acceleration in the cylindrical coordinate $\ddot{u}_r$. Red dashed line: $r\dot{\theta}^2$ computed from the angular velocity $\dot{\theta}$ measured by the gyroscope.

We can write the acceleration along the smartphone's y axis of Fig. 1 in terms of the cylindrical coordinates:

$$\begin{aligned} \vec{y} &= \sin\theta_a\ \hat{u}_r + \cos\theta_a\ \hat{u}_\theta \\ \ddot{\vec{y}} &= -\,r_a\dot{\theta}^2\sin\theta\ \hat{u}_r + r_a\ddot{\theta}\cos\theta\ \hat{u}_\theta \end{aligned}, \tag{17}$$

where $\hat{u}_r$ and $\hat{u}_\theta$ are the radial and angular cylindrical directions, respectively. When plotting the acceleration along the y axis for the pendulum, we observe that it is always negative (see black line in Fig. 3), which shows that $\theta_{acc} \approx \pi/2$, i.e., the accelerometer is positioned along the y axis. Hence, we can relate the measurements of the accelerometer and gyroscope by

$$\ddot{\vec{y}} = -r_a\dot{\theta}^2\hat{u}_r. \tag{18}$$

The value of r_a can be found then by minimising the distance between the signals for $\ddot{y}$ and $r_a\dot{\theta}^2$ for the motion of the pendulum[21]. Figure 3 shows in red the signal of $r_a\dot{\theta}^2$ that minimises such distance. We estimated through this method $r_a \approx 3.3\,\text{cm}$.

C. Normal modes

As shown by Berg and Marshal[19], the conditions $z_0 = \pm\theta_0\sqrt{I/m}$ set the system to oscillate in the symmetric and asymmetric normal modes, with $z_0 =$ 0.1m spacing. For these initial conditions, the simultaneous rotational and translational accelerations are shown in Fig. 4, where we can see them in phase for the symmetric mode (panel a) or in anti-phase for the asymmetric mode (panel b). Here, we calculate the rotational acceleration as the numerical gradient of the angular velocity measured by the smartphone. For both acceleration signals, we remove the DC components and apply a band-pass frequency filter between 0.1 to 1 Hz[22]. Attenuation is clearly visible along the twenty cycles represented in Fig. 4. We estimate the two normal mode frequencies from the discrete Fourier transform of the recorded signals for realisations with different initial conditions, obtaining $f_1 = \frac{\omega_1}{2\pi} = 0.539 \pm 0.003$Hz and $f_2 = 0.407 \pm 0.001$Hz, respectively. The uncertainties correspond to the standard deviations among realisations. The fundamental and beat frequencies can be estimated from f_1 and f_2 via Eq. (21).

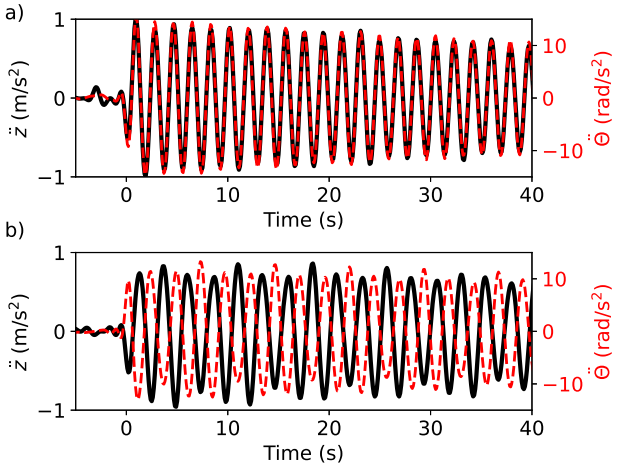

FIG. 4. Normal modes of the Wilberforce pendulum observed experimentally in the acceleration signals. a) Symmetric (first) mode observed in the accelerations $\ddot{z}(t)$ (red dashed line) and $\ddot{\theta}(t)$ (black line). b) Anti-symmetric (second) mode.

D. Beating observation

According to Eq. **??**, setting the initial conditions that correspond to beating for the translational and rotational positions, namely $z_0 = 0.82\,\text{m}$ and $\theta_0 = 0$, leads to partial beatings in the accelerations $\ddot{z}(t)$ and $\ddot{\theta}(t)$ (black line in Fig. 5 a). We obtain a good agreement between simulations –described in described in Sec. III E– and experimental data for the accelerations as a function of time and spectral density (dashed lines in Fig. 5 a) and b). To calculate the spectral density, we compute the discrete Fourier transform after applying a Blackman window to minimize side lobes. The amplitude ratio A_1/A_2 between the first and second modes are 0.52 ± 0.03 and 0.57 ± 0.03 for respectively the experiment and the numerical simulation. Both are in agreement with the theoretical prediction $\omega_1^2/\omega_2^2 = 0.57 \pm 0.01$ of Sec. II B. The experimental estimation is in agreement with . Uncertainties are estimated using the formula $\sigma =$

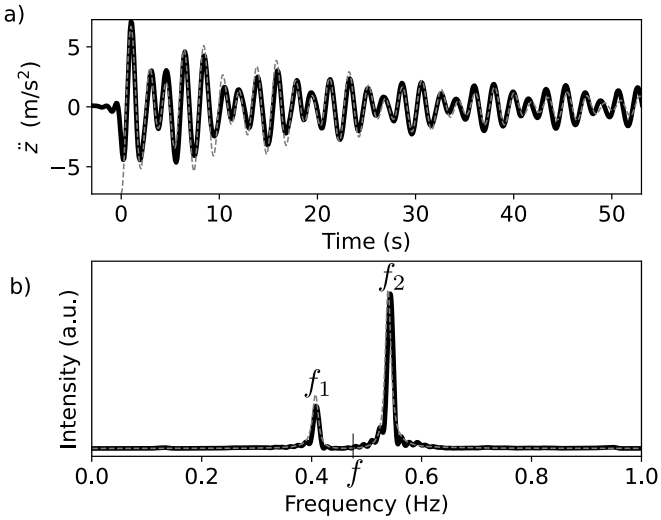

FIG. 5. Acceleration along the z-axis for initial conditions that ensure beating in the positional signals: $z_0 = 0.82\,\mathrm{m}$ and $\theta_0 = 0$. The experimental acceleration as a function of time in is represented in a) with black line. The numerical experiment is in grey dashed line. The corresponding spectral densities are plotted in b). At the first and second resonances, respectively f_1 and f_2 The ratio between the amplitudes is ω_1^2/ω_2^2 as per Eq. (13). The central frequency is indicated as f.

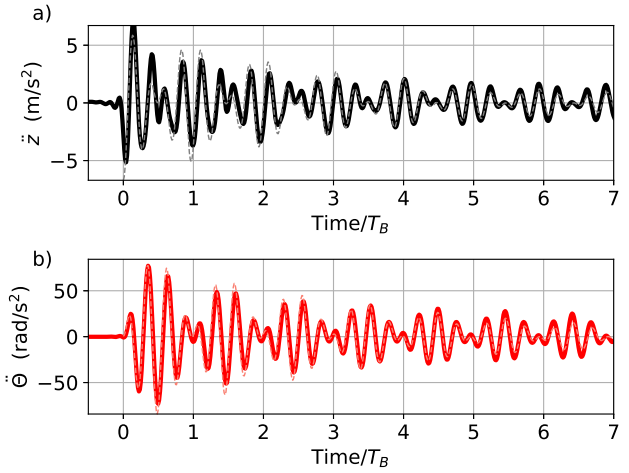

FIG. 6. Translational and rotational accelerations for initial conditions that ensure beats in the acceleration signals. a) Translational acceleration for initial conditions $z_0 = 0.82\,\mathrm{m}$ and no initial torque ($\theta_0 = -3.2\,\mathrm{rad}$). b) Rotational acceleration around z-axis for the same initial conditions as a). The time is rescaled to beating time $T_B = 7.6$ s, to facilitate the visualisation of the phase difference between the rotational and translational accelerations. The experimental measurements (solid lines) are in agreement with the numerical experiments (dotted lines).

FWHM$/2\sqrt{2\ln 2}$, where FWHM represents the full width at half maximum. This calculation assumes that the frequency peak follows locally a normal distribution, with σ representing the corresponding standard deviation. The peak frequency differences between experimental data and simulations are less than 0.5%. To obtain perfect beating on the acceleration time series, however, we need to impose the no-initial-torque condition (see Sec. II B).

When we set the initial conditions to no initial torque (in our case $z_0 = 0.82\,\mathrm{m}$, $\theta_0 = -\frac{\epsilon z_0}{2I\omega^2} = -3.2\,\mathrm{rad}$), we observe experimentally perfect beating in the rotational and translational accelerations (Fig. 6). Note that setting the initial angle θ_0 to its theoretical value is not needed, because we set up the pendulum by lifting it with one finger until it can rotate freely, thus satisfying the no-initial-torque condition. Simulations of the pendulum's motion equations with the same initial conditions are in good agreement with the experimental data (dotted lines in Fig. 6 a) and b). The observed phase difference between the translational and rotational accelerations, which is in agreement with Eq. (14), illustrates the energy exchange between translational and rotational motions. Our simulations predict both normal frequencies to have the same contribution to the spectrum of the rotational and translational accelerations (dotted lines in Fig. 7). However, the experimental amplitude ratio between the first and the second mode is $A_1/A_2 = 0.82$ for both acceleration types. Such disagreement between experiment and simulations is consistent with a 1.3 % difference between ω and the resonant frequencies ω_θ and ω_z, as explained in the following section.

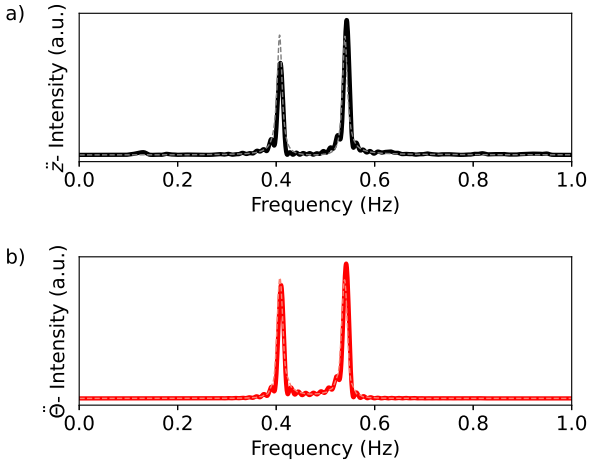

FIG. 7. Spectral densities for initial conditions that ensure beatings in the translational (panel a) and rotational (panel b) accelerations. In the simulation (dashed lines), the amplitude of the first and the second resonances coincide, in agreement with Eq. (14). The experimental components (full lines) are slightly different, having a ratio of 0.82.

E. Numerical experiments

To solve numerically the set of Equations (16), we rewrite the autonomous system in the form $\dot{\mathbf{X}} = f(\mathbf{X})$, where $\mathbf{X}$ is a vector quantity. Since the coupling term in our system is linear with respect to the translational and rotational positions, the motion equations form a linear system. Defining the new variables $r = \dot{z}$ and $s = \dot{\theta}$, the motion equations read

$$\begin{cases} \dot{r} = -(\omega_z^2)z - (\epsilon/2m)\theta - (\alpha_z/m)r \\ \dot{s} = -(\omega_\theta^2)\theta - (\epsilon/2I)z - (\alpha_\theta/I)s \end{cases} . \tag{19}$$

We can thus define $\mathbf{X} = (\mathbf{z}, \theta, \mathbf{r}, \mathbf{s})$, to express the motion equations as $\dot{\mathbf{X}} = \mathcal{M}\mathbf{X}$, where the matrix $\mathcal{M}$ is defined by

$$\mathcal{M} = \begin{bmatrix} 0 & 0 & 1 & 0 \\ 0 & 0 & 0 & 1 \\ -\omega_z^2 & -\epsilon/2m & -\alpha_z/m & 0 \\ -\epsilon/2I & -\omega_\theta^2 & 0 & -\alpha_\theta/I \end{bmatrix} . \tag{20}$$

Naturally, the solution for this system is given by $\mathbf{X}(\mathbf{t}) = \mathbf{e}^{\mathcal{M}}\mathbf{X}(\mathbf{0})$, and an analytical solution can be expressed in terms of the eigenvalues and eigenvectors of $\mathcal{M}$. If the eigenvalues and eigenvectors of $\mathcal{M}$ are not simple to calculate, they can be computed numerically.

We apply a classical, order 4 Runge-Kutta method to numerically calculate the solution of $\dot{\mathbf{X}} = \mathcal{M}\mathbf{X}$. The Python code, available in GitHub, uses the package *odeint* of *scipy* and is adapted from[23]. Note that the equations of motion assume the same conditions of the theoretical analyses in Sec. II, including equal attenuation for the rotational and translational oscillations. We estimate the simulation parameters from the experimentally measured normal frequencies, mass and inertia, namely

$$\begin{aligned} \omega &= \sqrt{\frac{\omega_1^2 + \omega_2^2}{2}}, \\ \omega_B &= \sqrt{\frac{\omega_1^2 - \omega_2^2}{\omega}}, \\ \epsilon &= 2\omega\omega_B\sqrt{mI}. \end{aligned} \tag{21}$$

These expressions assume the simplification of Eq. (7) with $\omega_B/\omega = 0.27$. Such simplification induces an error that is smaller than 1%. Nevertheless, this error accumulates period after period, and the time shift is visually noticeable after 10 periods. We thus strongly recommend using, instead, the full expression of Eq. (21). We estimate the damping factor $\zeta = 0.013$ is by minimising the difference between the numerical and experimental data.

The numerically-calculated time series and spectral densities in Figs. 5 to 7 use the perfect tuning hypothesis ($\omega_z = \omega_\theta$). We can investigate the effects of frequency detuning through the simulations by adding a detuning parameter ε between the resonant frequencies as follows: $\omega_z = (1+\varepsilon)\omega$ and $\omega_\theta = (1-\varepsilon)\omega$. Interestingly, setting $\varepsilon = 0.013$ yields the same amplitude ratio observed in Fig. 7 ($A_1/A_2 = 0.82$). This estimation of the detuning parameter ε allows to quantify the difference between the independant and coupled resonances:

$$\frac{\omega_\theta - \omega_1}{\omega} = \frac{\omega_2 - \omega_z}{\omega} \approx 0.13 \tag{22}$$

Moreover, for such detuning the time series remains visually unchanged and the frequency spectra of both simulation and experiments are in agreement (Fig. 8). Notably, detuning the resonant frequencies does not change the coupled system frequencies ω_1 and ω_2. The difference between the resonance frequency being given by

$$\frac{\omega_z - \omega_\theta}{\omega} = 2\epsilon \approx 0.026 \tag{23}$$

indicates that the perfect tuning hypothesis adequately describes the normal frequencies and beats. Nevertheless, detuning is necessary to explain the relationship between the amplitudes in the frequency spectrum.

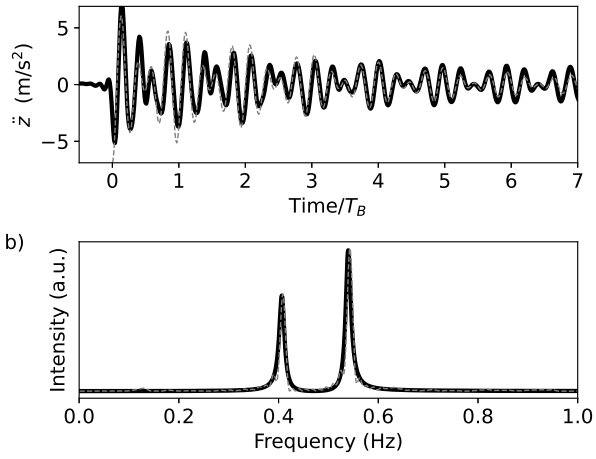

FIG. 8. Comparison between the experimental acceleration signals of Figs. 6 a) and 7 a) (continuous line), and a numerical simulation (dashed line) taking into account the frequency difference $\omega_z = (1+\varepsilon)\omega$ and $\omega_\theta = (1-\varepsilon)\omega$, with $\varepsilon = 0.013$.

IV. SUMMARY AND DISCUSSION

In this work we have proposed a simple and low-cost setup for the study of the Wilberforce pendulum. By attaching a smartphone to the pendulum, we measured the acceleration and angular velocity via the accelerometer and gyroscope of the device. Supported by numerical solutions to the motion equations (Sec. III D), we studied quantitatively the normal modes (Sec. III

B) and beat conditions (Sec. III C) of the system, obtaining a remarkable agreement between experiments and numerical results (Figures 4 to 7).

Notably, our experimental setup measures the motion with respect to a frame of reference attached to the pendulum. This feature simplifies the analysis and sheds light on the optimum technique for setting the initial conditions to obtain perfect beatings in acceleration (Sec. II C). In contrast, with setups based on filming the motion of the pendulum, measurements in the frame of reference of the pendulum can only be indirectly calculated from data obtained in the earth's frame of reference[3].

The Wilberforce pendulum can be a valuable asset for laboratory courses or as a demonstration of coupled oscillations in university physics courses. The analysis of its motion involves critically reviewing key concepts in physical sciences, such as normal modes, coupled systems, cylindrical coordinates or relative motion. Moreover, the experimental study of the pendulum can serve as an ideal gateway to data analysis techniques such as the fast Fourier transform and data filtering, as well as to numerical methods for ordinary differential equations.

The simplicity of our experimental setup stems from the use of a smartphone as our measuring device, rendering the study of the Wilberforce pendulum easily reproducible. All the numerical tools we use in this study are freely available online. In addition, we provide our datasets and Python scripts we used to analyse the experimental data and perform numerical experiments.

Data accessibility

Numerical simulation, data sets and data analysis are freely available at GitHub repository.

Acknowledgements

This research was supported by the Ministerio de Educación y Cultura with the grant "Fondo Vaz Ferreira" (II-FVF-2019-145). The authors thank the lockdown measures for keeping them isolated with a spring and a candy box as their main source of amusement.

Conflict of interest declaration

The authors have no conflicts to disclose.

* tgallot@fisica.edu.uy
† dgau@fing.edu.uy
‡ rodrigo.garcia@ed.ac.uk

[1] Lionel Robert Wilberforce. Xliv. on the vibrations of a loaded spiral spring. *The London, Edinburgh, and Dublin Philosophical Magazine and Journal of Science*, 38(233):386–392, 1894.

[2] E Debowska, S Jakubowicz, and Z Mazur. Computer visualization of the beating of a wilberforce pendulum. *European journal of physics*, 20(2):89, 1999.

[3] T Greczylo and E Debowska. Using a digital video camera to examine coupled oscillations. *European journal of physics*, 23(4):441, 2002.

[4] Giacomo Torzo and Michele D'Anna. The wilberforce pendulum: a complete analysis through rtl and modelling. *Quality Development in Teacher Education and Training*, pages 579–585, 2004.

[5] Pierre Devaux, Valentin Piau, Ombeline Vignaud, Guillaume Grosse, Renato Olarte, and Alexis Nuttin. Cross-camera tracking and frequency analysis of a cheap slinky wilberforce pendulum. *Emergent Scientist*, 3:1, 2019.

[6] Matthew Mewes. The slinky wilberforce pendulum: a simple coupled oscillator. *American Journal of Physics*, 82(3):254–256, 2014.

[7] Miro Plavcic and Pasko Zupanovic. The resonance of the wilberforce pendulum and the period of beats. *Latin-American Journal of Physics Education*, 3(3):8, 2009.

[8] CJ Pereyra, M Osorio, A Laguarda, and DL Gau. Fourier analysis of a vibrating string through a low-cost experimental setup and a smartphone. *Physics Education*, 53(4):045019, 2018.

[9] M Osorio, CJ Pereyra, DL Gau, and A Laguarda. Measuring and characterizing beat phenomena with a smartphone. *European Journal of Physics*, 39(2):025708, 2018.

[10] Álvaro Suárez, Daniel Baccino, Martín Monteiro, and Arturo C Martí. Normal coordinates in a system of coupled oscillators and influence of the masses of the springs. *European Journal of Physics*, 42(1):015003, 2020.

[11] Martin Monteiro, Cecilia Stari, Cecilia Cabeza, and Arturo C Marti. Physics experiments using simultaneously more than one smartphone sensors. In *Journal of Physics: Conference Series*, volume 1287, page 012058. IOP Publishing, 2019.

[12] Martín Monteiro, Cecilia Stari, Cecilia Cabeza, and Arturo C Marti. A bottle of tea as a universal helmholtz resonator. *The Physics Teacher*, 56(9):644–645, 2018.

[13] Jochen Kuhn and Patrik Vogt. Analyzing spring pendulum phenomena with a smart-phone acceleration sensor. *The Physics Teacher*, 50(8):504–505, 2012.

[14] David Weiler and Arne Bewersdorff. Superposition of oscillation on the metapendulum: Visualization of energy conservation with the smartphone. *The Physics Teacher*, 57(9):646–647, 2019.

[15] Katrin Hochberg, Jochen Kuhn, and Andreas Müller. Using smartphones as experimental tools—effects on interest, curiosity, and learning in physics education. *Journal of Science Education and Technology*, 27(5):385–403, 2018.

[16] Gallot Thomas. Github repository for data analysis and simulation of the wilbuerforce pendulum, 2022.

[17] Ulrich Köpf. Wilberforce's pendulum revisited. *American Journal of Physics*, 58(9):833–837, 1990.

[18] CJ Ancker. Pitch and curvature corrections for helical springs. *J. Appl. Mech.*, 25:466–470, 1958.

[19] Richard E Berg and Todd S Marshall. Wilberforce pendulum oscillations and normal modes. *American Journal of Physics*, 59(1):32–38, 1991.

[20] Stampfer Christoph, Heinke Heidrun, and Staacks Sebastian. A lab in the pocket. *Nature Reviews. Materials*, 5(3):169–170, 2020.

[21] Chris Isaac Larnder. A purely geometrical method of locating a smartphone accelerometer. *The Physics Teacher*, 58(1):52–54, 2020.

[22] The scipy.signal has a *detrend* function, a Butterworth filter coefficient design (*butter*) and [textitsosfiltfilt to apply the filter in the time domain.

[23] Christian Hill. Scipython: The willburforce pendulum, 2015.